Proceedings of the Canadian Society for Mechanical Engineering International Congress
32nd Annual Conference of the Computational Fluid Dynamics Society of Canada
Canadian Society of Rheology Symposium
CSME-CFDSC-CSR 2025
May 25–28, 2025, Montréal, Québec, Canada

FUNCTIONAL PERFORMANCE OF RECTANGULAR RIBLET-STRUCTURED SURFACES IN WATER-GLYCEROL MIXTURE: EFFECT OF RIBLET HEIGHT

Joshua Fritz[1], William B. Gordon[1,2], Jennifer Oliva[1,2],
O. Remus Tutunea-Fatan[1,2*], Evgueni V. Bordatchev[2,1**]
[1]Department of Mechanical and Material Engineering, Western University, London, Canada
[2]Automotive and Surface Transportation, National Research Council of Canada, University, London, Canada
*rtutunea@eng.uwo.ca, **evgueni.bordatchev@nrc-cnrc.gc.ca

Abstract— This study investigates the influence of riblet height on drag reduction by means of Taylor-Couette system employing a water-glycerol mixture. For this purpose, structured surfaces with rectangular riblets characterized by depths of 25 µm, 45 µm, and 65 µm fabricated through high-precision micromachining were evaluated against a smooth surface baseline. Preliminary results showed that 25 µm riblets achieved a modest drag reduction (~0.5%), while deeper riblets (45 µm and 65 µm) increased drag likely due to vortex trapping. The analysis of the torque confirmed that 65 µm riblets stabilized the flow but induced localized turbulence. Taken together, these findings highlight the potential of microstructured functional surfaces for energy-efficient hydrodynamic and aerodynamic applications.

Keywords-drag reduction; functional surface; rectangular riblets; functional performance; Taylor-Couette system; analysis

I. INTRODUCTION

Past studies have shown that the addition of carefully designed arrays of microstructures onto a surface has the potential to significantly enhance its functional properties, leading to improved performance, durability, and efficiency across various scientific and engineering applications. More specifically, microstructures/microtextures can significantly boost the functional properties of a surface such as hydrophobicity, self-cleaning, friction control, hydro- and aero-dynamics and therefore they could have important downstream effects in aerospace, automotive, energy, military, and biomedical industries [1, 2]. However, optimal microstructure design continues to pose challenges primarily due to the limited understanding of the interactions between the fluid/media and texture. Furthermore, the manufacturing of microstructures characterized by complex designs often elevates the complexity of the problems to be tackled [3].

Over the past few decades, microriblets have been the focus of extensive research, involving various designs and manufacturing processes to showcase their commercial potential. Along these lines, various geometric designs and sizes have been explored [4], including biomimetic structures like sharkskin, simple geometric shapes like circles or triangles as well as unique designs [5]. Nonetheless, the functional performance of many of these designs continues to be difficult to evaluate due to experimental and numerical modeling challenges/limitations [4, 6].

While a wide variety of streamwise riblet profiles exists [4], triangular and rectangular designs tend to be more used for hydro- and aero-dynamic applications mainly because they can be fabricated easily and precisely. In fluid dynamics applications, drag reduction generally translates into energy savings and improved efficiency. In addition to drag reduction, riblet microstructures enhance hydrophobicity by trapping air in grooves, repelling water and contaminants. While fabrication techniques such as CNC machining, laser ablation, and lithography enable precise production, challenges in scalability, durability, and cost-effectiveness persist [7].

Among these designs, those replicating or at least mimicking sharkskin microstructures remain significant since it was shown that continuous riblets can reduce drag by 10% compared to a smooth surface [8]. This significant drag reduction arises because streamwise vortices are lifted, thereby reducing transverse shear stresses. Typically, each form parameter of the riblet design, such as spacing s, height h, and thickness t, are nondimensionalized to become viscous-scaled parameters s^+, h^+, and t^+, respectively. This transformation enables the adaptability and scalability of the design parameters with respect to the application medium. Therefore, the use of s^+, h^+, and t^+ facilitates the employment of design principles and considerations required to achieve an optimal functional performance.

The phenomenological model of surface drag is linked to the dynamic interactions between surface microasperities and fluid vortices. In the most common case, less contact area leads to

This research was funded by the Natural Science Engineering Research Council of Canada under grants RGPIN/6616-2019 and RGPIN/5126-2019.

drag reduction. For this reason, riblets are added to a surface to reduce the fluid-surface contact area by moving this interface away from the smooth surface and towards the top of the riblets.

It has been proven by CFD numerical simulation and experimental results [8] that optimal drag reducing s^+ values should be ~15-20 for lifting the vortices up away from the riblet-structured surface. If riblets are too tall, media vortices will be trapped around the riblets, increase the contact area and therefore flow drag over the entire surface. Riblets that are too short will be incapable to push the vortices away from the surface to decrease sweeps and ejections since the contact area will be extended to include both smooth surface and riblet walls. The suggested optimal h^+ values are approximately 8 to 10. Drag reduction generally occurs when vortices are located above the riblet peaks and because of this, thinner riblets are more desirable. On the other hand, these riblets play a smaller role in drag change since they do not affect by much the fluid-surface interface area. Streamwise rectangular riblets have been shown to significantly reduce drag in turbulent flows, achieving reductions up to 10% under optimal conditions [9]. Their geometry disrupts large turbulent eddies, maintaining smaller, stable vortices that reduce skin friction and energy loss. A key parameter in this regard is represented the spacing-to-height ratio, whose optimal values are typically between 10 and 15 [9].

This study investigates the functional performance of surfaces with rectangular riblets immersed in a water-glycerol mixture. The study focuses on the effect of riblet height variations on torque as measured by a Taylor-Couette system. For this purpose, three torque components (mean, kinematic, and dynamic) were analyzed and compared.

II. Microfabrication Procedure

In this study, single point diamond cutting (SPDC) was used to fabricate an array of rectangular riblets on an outer cylindrical surface. The SPDC operations were performed on a MICROGANTRY nano5X system (Kugler GmbH, Salem, Germany) [10] that encompasses sophisticated micromachining capabilities such as micromilling with spindle speeds of up to 125,000 rpm, fly cutting up to 2,000 rpm, as well as laser irradiation for material ablation or melting purposes. A Renishaw™ touch probe – offering a measurement accuracy of ±500 nm – can be used to assess the workpiece geometry before, during, and after machining, as well as for alignment purposes. Furthermore, the system features a Blum™ tool-setting sensor that can be used to measure cutting tool geometry (diameter and length) with a repeatability of $2\sigma = 100$ nm. The motion stages operate on air bearings with a positional resolution of 10 nm and positional accuracy of ±250 nm in the X-Y plane and ±500 nm along the Z axis. The straightness is maintained within ±800 nm per 100 mm of translation for all linear axes. Furthermore, the system is equipped with a Duetto picosecond laser (Time-Bandwidth Products, Inc., Switzerland), characterized by a maximum average power of 12 W, pulse width of 10.5 ps, repetition rate of up to 8.2 MHz, and 1064 nm wavelength.

In the context of this study, a cylindrical workpiece was securely mounted on the A/C-axis tilt/swivel motion stage and aligned along the X and Z axes with a ±250 nm accuracy by means of the Renishaw™ touch probe. The rectangular grooves were machined on the outer surface of the cylindrical acrylic workpiece (drum) by means of a SPDC tool with a 100 µm width, similar to those used to fabricate retroreflective microoptics [11].

Fig. 1 shows the microfabrication setup (Fig. 1a) and sample drum exhibiting rectangular riblets (Fig. 1b). Each acrylic disk (76.2 mm diameter, 12.7 mm thickness) was mounted on the A/C-axis tilt/swivel stage and aligned as precise as possible (vertically and radially) to ensure minimum deviations from the center of rotation. After that, four cylindrical samples were fabricated as follows: one with a smooth surface and three characterized by a spacing of 150 µm, a thickness of 50 µm and three different heights (25 µm, 45 µm, and 65 µm). All four samples ended up having different outer diameters (75.62 mm, 75.84 mm, 76.01 mm, and 75.87 mm).

All cylindrical samples were structured by performing a vertical cutting operation. The resulting structure shape and surface topography were examined using an optical interferometer, namely WYKO NT1100 (Veeco, Ltd., USA), that is characterized by a vertical resolution of 0.1 nm and an X-Y grid size of 192.98 nm. The 3D topography of the structured surface with rectangular riblets of 45 µm in height is shown in Fig. 2a whereas its cross-section is illustrated in Fig. 2b. The inspection of the geometry shows minor dimensional deviations from nominal values: 1.6 µm for spacing, 0.5 µm for thickness, and 0.2 µm for height. The fabricated riblets were straight, undeformed, characterized by a superior surface quality (inspectable under a certain tilting angle) as well as minimum burr formation.

III. Taylor-Couette Experimental Setup

The methods and instruments involved in the experimental evaluation of the performance for riblet-structured functional surfaces represent critical components of the research. Along these lines, one of the most used methods to assess the aerodynamic performance of structured surfaces relies on wind tunnels that are, however, sizeable and costly. During wind tunnel testing, the synergetic effects of aerodynamic shape and fluid-surface interactions play an important role on the overall aerodynamic performance. Because of this, the separation of the two factors constitutes a challenging task. Nonetheless, past studies [3, 4] seem to suggest that the well-established Taylor-Couette systems could provide a cost-efficient, easy-to-use, reliable, and efficient solution for the evaluation of the functional performance of riblet-structured surfaces [8, 12, 13], particularly when integrated with particle image velocimetry measurements [14].

Building on these observations, the Taylor-Couette system employed in this study (Fig. 3) serves as a relatively new method for analyzing the functional performance of structured surfaces. For this purpose, the Kinexus Pro+ rheometer (Malvern Instruments Ltd.) was used to conduct Taylor-Couette flow measurements under the azimuthal Couette flow and axisymmetric toroidal Taylor vortices, and von Kármán flow regimes [15, 16]. The key component of the rotational device is represented by a high-precision spindle mounted on air bearings, capable of rotating at angular velocities ranging from 10 nrad/s to 500 rad/s. The apparatus includes three essential sensors that provide real-time, synchronous measurements for: i) applied torque, ranging from 10 nN·m to 200 mN·m with the resolution

of 0.1 nN·m, ii) angular position during rotation with the resolution of less than 10 nrad, and iii) normal force, ranging from 0.001 N to 20 N with a resolution of 0.5 mN.

A Taylor-Couette (T-C) cell was constructed of two coaxially allocated components – an immobile external cylindrical container and a rotational drum. The container was fabricated from an acrylic tube having a smooth inner surface and with an outer diameter of 101.6 mm whereas the inner diameter was 88.9 mm. The total height, wall thickness, and base thickness were set at 76.2 mm, 6.35 mm, and 12.7 mm, respectively. During the experiments, each textured cylindrical sample (drum) was connected to the rheometer spindle and precisely positioned 10 mm above base level. The T-C cell was closed off with a top lid penetrated by a central hole for the spindle shaft as well as to prevent the overflow of the fluid (50-50% glycerol-water mixture) between drum and container. By accounting for all design parameters of the T-C cell, the radius ratio is $\eta = R_{drum}/R_{container} = 0.853$ whereas the height ratio ended up being $\Gamma = L_{drum}/(R_{container} - R_{drum}) = 0.977$.

IV. Functional Performance Analysis

During hydrodynamic performance evaluation, the drum attached to the spindle was rotated within a preset range of angular speeds ranging from 4.8 rad/s to 152.0 rad/s in 10.2 rad/s increments. As expected, rotation of the drum creates inner volumetric shear flows and instabilities within the fluid causing in turn dynamic frictional torque responses. The torque response also correlates with the drag in the cylindrical region of the T-C cell, but it is also affected by an additional contribution from the von Kármán flow that occurs at the bottom of the drum. During the experiments, the data collected by the built-in rheometer sensors – time (s), angular position (deg), torque (μN·m) – was acquired with a 1 kHz framerate. Each drum was tested in triplicate in presence of a 50-50% water-glycerol mix. The mass of each drum was normalized before tests began.

After experiments were completed under controlled shear rate and stress regimes, the data acquired was stored in a file for further analysis of the rheological properties of fluid-surface interaction dynamics. Following this, in-house developed comprehensive MATLAB-based functions were written and used for plotting all data in time domain (angular speed and torque) and for determining statistical parameters (mean and standard deviation, STD) as well as functions (amplitude-frequency A-F and probability density PD).

Given the large dataset (66,021 records per parameter), this study focuses on a single angular speed (63.7 rad/s) for a detailed preliminary analysis and methodology development. Of note, the change of angular speed was always accompanied by transient behaviour. More specifically, the angular speed will increase after torque has reached a steady state for at least 10 seconds. However, this transient data range was excluded from further analysis. Also, the most common experimental challenge in any T-C setup is caused by the additional torque yielding from the no-slip boundary condition that is developed between the floor of the container and the bottom of the drum.

This study constitutes a logical development of our past work [13, 17] performed for the same drums but immersed in water instead. As previously indicated, the measured torque $Q(t)$ can be represented as a linear combination of three components - constant (mean value), periodic (quasi-dynamic), and dynamic - as follows:

$$Q(t) = \bar{Q} + \hat{Q}(t) + \tilde{Q}(t), \quad (1)$$

where $Q(t)$ is the measured torque value, $\bar{Q}$ is the mean torque, $\hat{Q}(t) = A \sin(\omega t)$ is the periodic component with the amplitude A and the frequency of rotation ω, and $\tilde{Q}(t)$ is the dynamic component induced by the hydrodynamic interactions at the surface-liquid interface. The statistical parameters of these components are presented in Table I as estimations of the functional performance.

TABLE I. Parameters Of Functional Performance

Parameters		Depth of rectangular riblets			
		0 μm (smooth)	25 μm	45 μm	65 μm
$Q(t)$	Mean, μN·m	7.864	7.853	8.126	7.997
	STD, μN·m	0.188	0.183	0.183	0.176
	Max A-F amplitude, μN·m/Hz	0.196	0.220	0.239	0.228
$\hat{Q}$	Magnitude, μN·m	0.567	0.567	0.583	0.567
	STD, μN·m	0.164	0.165	0.173	0.165
$\tilde{Q}$	Magnitude, μN·m	0.348	0.360	0.388	0.531
	STD, μN·m	0.045	0.045	0.044	0.045

Table I shows that only the 25 μm tall riblets achieved a lower $\bar{Q}$ than the smooth sample. This suggests the presence of a small drag reduction (~0.5%). However, the minimum $Q_{STD}(t)$ is observed for 65 μm riblets corresponding to the most stable liquid-surface interface that is characterized by the least amount of torque variations. The performance of $\hat{Q}(t)$ is quite repeatable for all drums, but 45 μm sample exhibits the highest values in terms of magnitude and STD. The performance of $\tilde{Q}(t)$ is also consistent in terms of STD. Nonetheless, $\tilde{Q}(t)$ shows a consistently increasing trend from the smooth to sample with the tallest riblets.

A more detailed and comprehensive analysis of $\bar{Q}$, $\hat{Q}(t)$, and $\tilde{Q}(t)$ is shown in Figs. 4-7, in which the actual torque $Q(t)$, zoomed-in $Q(t)$, $\hat{Q}(t)$, $\tilde{Q}(t)$, A-F characteristic of $Q(t)$, and PD function of $\tilde{Q}(t)$ are depicted. The qualitative analysis of all plots reveals a visible increase in mean torque for all samples except for the 25 μm one, when compared to the baseline smooth riblet geometry. This reinforces the previous comment that a moderate decrease in drag is associated with the 25 μm riblets.

Each A-F characteristic has two distinct frequency sections, namely a dominant frequency at $\omega/2\pi$ and a low-frequency range of $]0, \omega/2\pi[$. This observation supports the underlying assumption for three components of $Q(t)$. The analysis of each A-F characteristic confirms that the source of $\hat{Q}(t)$ can be attributed to the lack of coaxiality between spindle, shaft, drum, and container (caused by manufacturing and assembly imperfections). For this reason, the parameters of $\hat{Q}(t)$ (mean and STD) are relatively consistent except for the 45 μm sample that has highest amplitude of A-F characteristic (Fig. 6e). It is also evident that the dominant frequency will be constant for all experiments with equal rotating speed, but its amplitude will change according to the accuracy and precision of the spindle-shaft-drum-container assembly and will not be notably affected by the liquid-surface interactions.

The dynamic component $\tilde{Q}(t)$ has its own representation in the A-F characteristic. The dynamics of the liquid-surface interactions is influenced by the interface between the structured surface and the turbulent fluid flows that correspond to the analyzed frequency range of $[0, \omega/2\pi]$. The amplitudes and their distribution in this frequency range will vary since it is affected by flow regimes, existent vortices, interface conditions as well as design parameters of surface structures. This is confirmed by the mean and STD values of $\tilde{Q}(t)$ presented in Table I. However, the frequency range of $[0, \omega/2\pi]$ requires a more comprehensive analysis since it contains the most relative and inclusive information about the dynamics of liquid-surface interactions. A particular attention should be given to the analysis of the PD function of $\tilde{Q}(t)$, since it serves as an indicator of predictability, randomness, variability, and chaoticity. The visual analysis of the PD function in Fig. 4f-7f implies that the $\tilde{Q}(t)$ data are tightly clustered around the mean for the 45 µm riblets (more than for the other geometries), and this correlates with a smaller variance (Table I).

V. Summary and Conclusions

This work presents preliminary findings about cylindrical drag-reducing surfaces featuring rectangular riblet grooves with depths of 25 µm, 45 µm, and 65 µm whose performances were compared with a smooth/non-grooved baseline. For this purpose, fabrication process and performance evaluation were also examined. To complete the trials, four acrylic drums were precision-machined by means of multi-axis SPDC since it enables high surface quality (< 2 µm form accuracy). One drum was left smooth (without grooves), while on the other three different riblet patterns (150 µm groove-spacing and 50 µm thickness) were fabricated. The drag reduction performance of each of the four cylindrical samples was assessed by means of a rheometer-derived Taylor-Couette system that was able to synchronously record torque, position, and force. The data acquired were used to analyze relationships between rotational position, torque, normal force, and speed. The analysis performed enabled the following conclusions:

- The preliminary results presented above seem to imply that the 25 µm tall riblets are capable of modest drag reductions (~0.5%, potentially suggesting an optimized range in which the wetted surface area is reduced while still disrupting turbulence and preventing vortex trapping.
- The decreased drag reduction performance associated with the 45 µm and 65 µm tall riblets suggest that once a maximum riblet height was exceeded, drag reduction is no longer effective. This idea is supported by the gradually increasing drag values compared to the 25 µm riblets as well as the smooth drum. The 65 µm tall riblets exhibited the highest dynamic torque magnitude and lowest minimum $Q_{STD}(t)$, thus indicating chaotic fluctuations in dynamic torque while maintaining a stable liquid-surface interface. While this may appear contradictory, it suggests that turbulent vortices were trapped between the riblets, stabilizing the overall flow despite local fluctuations. As a result, the 65 µm tall riblets help stabilize global flow but lose drag reduction efficiency due to increased energy dissipation and local turbulence.

Taken together, these findings serve as preliminary results, while providing a foundation for further investigation. Future extensions of this work will focus a narrower range of riblets around the 25 µm height.

Acknowledgment

The work presented in this study is the result of the collaboration between Western University (London, Ontario, Canada) and National Research Council of Canada.

References

[1] B. Bhushan and Y. C. Jung, “Natural and biomimetic artificial surfaces for superhydrophobicity, self-cleaning, low adhesion, and drag reduction,” Progress in Materials Science, 2011, 56(1), pp. 1-108.

[2] H.A. Abdulbari, H.D. Mahammed, and Z.B.Y. Hassan, "Bio-inspired passive drag reduction techniques: A review," ChemBioEng Reviews, 2015, 2(3), pp. 185-203.

[3] H.A. Abdulbari, R.M. Yunus, N.H. Abdurahman, and A. Charles, "Going against the flow—A review of non-additive means of drag reduction," Journal of Industrial and Engineering Chemistry, 2013, 19(1), pp. 27-36.

[4] M.R. Pakatchian, J. Rocha, and L. Li, “Advances in riblets design,” Applied Science, 2023, 13, paper 10893, 36 pp.

[5] S. Lee, H.M. Sheikh, D.D. Lim, G.X. Gu, and P.S. Marcus, "Bayesian-optimized riblet surface design for turbulent drag reduction via design-by-morphing with Large Eddy simulation." Journal of Mechanical Design, 2024, 146, paper 081701, 15 pp.

[6] B. Mele, "Riblet drag reduction modeling and simulation," Fluids, 2022, 7(7), paper 249, 15 pp.

[7] S. Zhang, Y. Zhou, H. Zhang, Z. Xiong, and S. To, “Advances in ultra-precision machining of micro-structured functional surfaces and their typical applications,” Int’l J of Mach Tools & Manuf, 2019, 142, 16-41.

[8] S. Martin and B. Bhushan, "Fluid flow analysis of continuous and segmented riblet structures," RSC Advances, 2016, 6(13), pp. 10962-78.

[9] A.J. Greidanus, R. Delfos, S. Tokgoz, and J. Westerweel, “Turbulent Taylor–Couette flow over riblets: drag reduction and the effect of bulk fluid rotation,” Experiments in Fluids, 2015, 56, paper 107, 13 pp.

[10] E.V. Bordatchev, M. Tauhiduzzaman, T. Kugler, A. Katz, and R. Bohr, “Demonstration of advanced capabilities of 5-axis micromilling: geometries with high-aspect ratio and/or optical surface quality,” Proc of the 8th Int’l Conf on Micro Manufacturing, 2013, pp. 357–362.

[11] N. Milliken, B. Hamilton, S. Hussein, O.R. Tutunea-Fatan, and E.V. Bordatchev, “Enhanced bidirectional ultraprecise single point inverted cutting of right triangular prismatic retroreflectors,” Precision Engineering, 2018, 52, pp. 158-169.

[12] M.S. Naim and M.F. Baig, “Turbulent drag reduction in Taylor-Couette flows using different super-hydrophobic surface configurations,” Physics of Fluids, 2019, 31, paper 095108, 18 pp.

[13] E.V. Bordatchev, W.B. Gordon, O.R. Tutunea-Fatan, N. Song, and L. Li, “Drag reducing functional surface with 60 degree riblets,” 2025, AIAA SciTech Forum, 2025, 10 pp.

[14] B. Xu, H. Li, X. Liu, Y. Xiang, P. Lv, X. Tan, Y. Zhao, C. Sun, and H. Duan, “Effect of micro-grooves on drag reduction in Taylor–Couette flow,” Physics of Fluids, 2023, 35, paper 043608, 10 pp.

[15] S.G. Huisman, R.C. van der Veen, C. Sun, and Lohse, D. "Multiple states in highly turbulent Taylor-Couette flow," Nat Com, 2014, 5, paper 3820

[16] A.J. Greidanus, R. Delfos, and J. Westerweel, "Drug reduction by surface treatment in turbulent Taylor-Couette flow," Journal of Physics: Conference Series, 2011, 318, paper, 082016, 9 pp.

[17] W.B. Gordon, E.V. Bordatchev, O.R. Tutunea-Fatan, N. Song, and L. Li, “Preliminary Evaluation of Drag Reduction Performance for Functional Surfaces with 60-degree Riblets Subjected to Taylor-Couette Flows,” Proc. 5th Int’l Conf on Fluid Flow and Thermal Sc, 2024, paper 159, 8 pp.

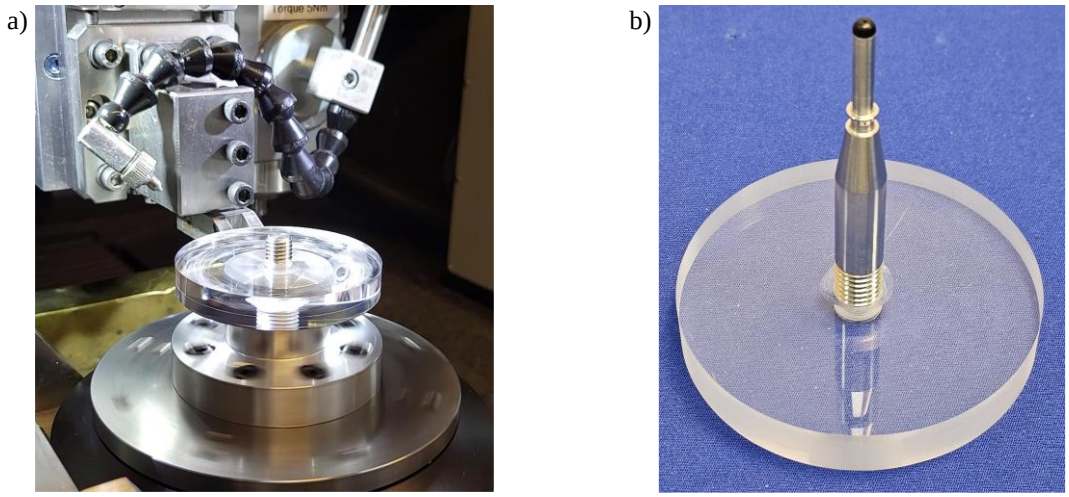

Figure 1. Overview of: a) microfabrication setup and b) microfabricated textured cylindrical sample (drum) with rectangular riblets.

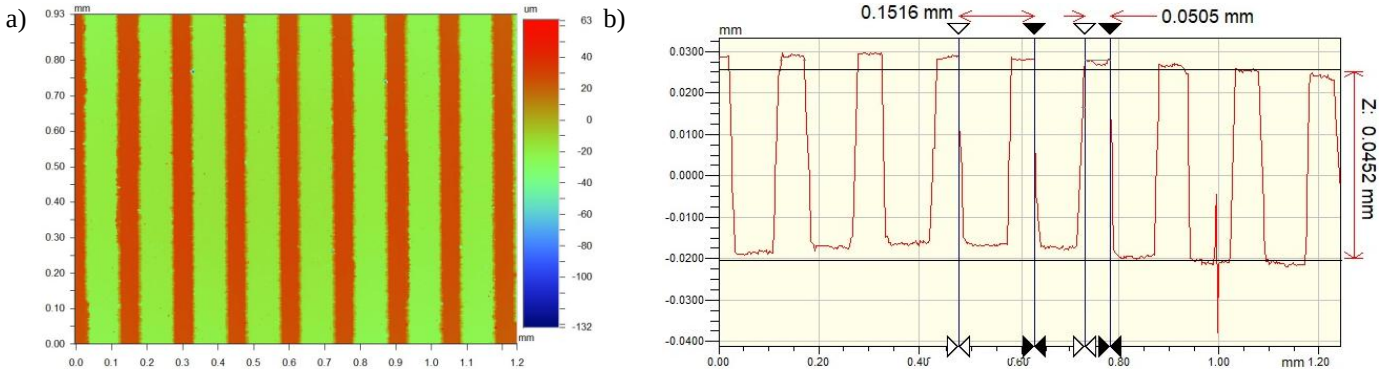

Figure 2. Example of form accuracy and precision for 45 µm riblets: a) 3D surface topography and b) assessment of form geometry.

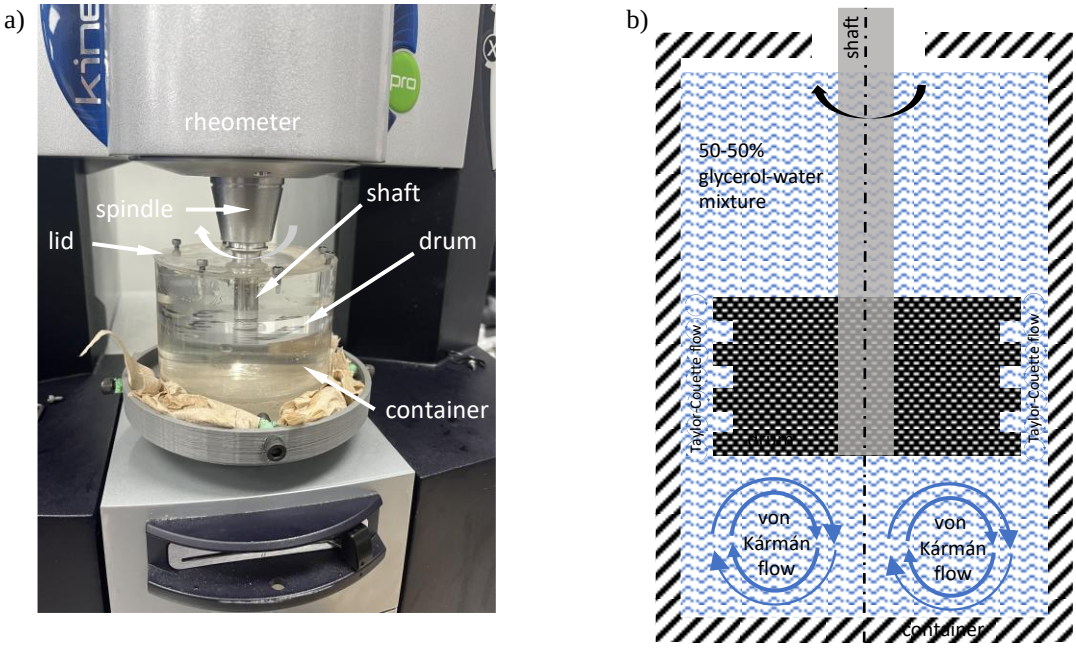

Figure 3. Rheometer-based Taylor-Couette system for functional performance evaluation: a) photo and b) schematic of Taylor-Couette cell.

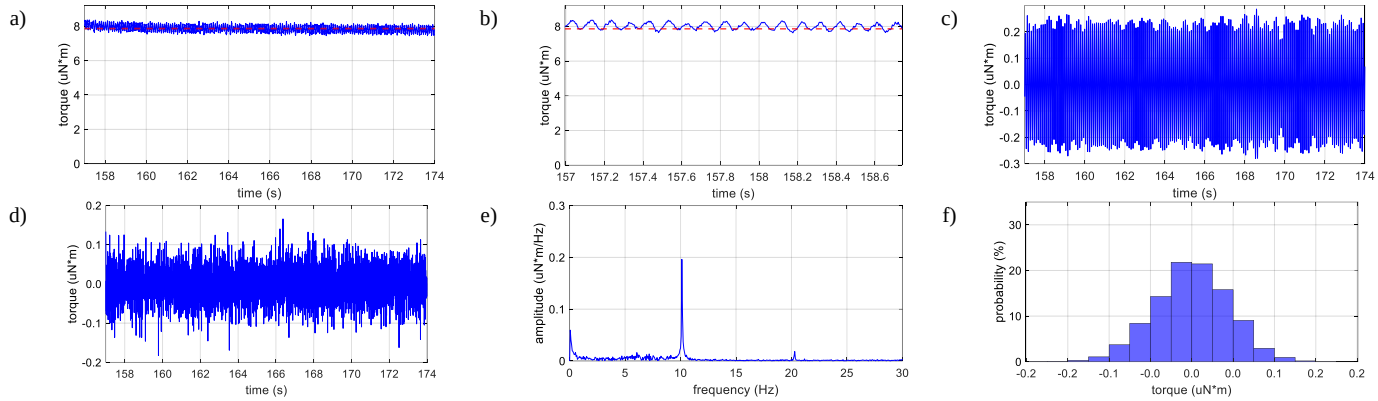

Figure 4. Functional performance of the drum with smooth surface at 63.7 rad/s angular speed: a) actual torque, b) detail view of the actual torque variation, c) torque kinematic component, d) torque dynamic component, e) AFC of actual torque, and f) PDF of actual torque.

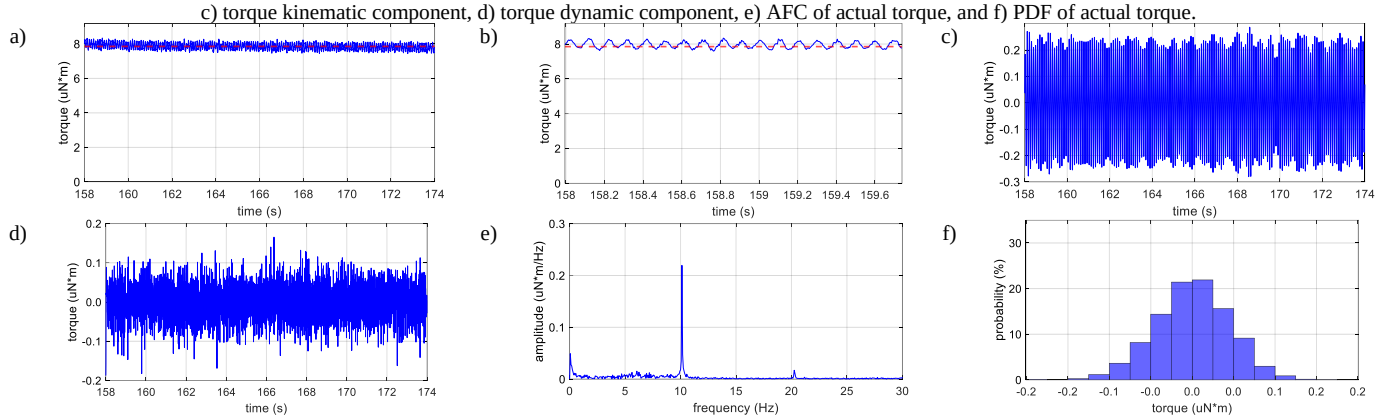

Figure 5. Functional performance of the drum with 25 µm riblets at 63.7 rad/s angular speed: a) actual torque, b) detail view of the actual torque variation, c) torque kinematic component, d) torque dynamic component, e) AFC of actual torque, and f) PDF of actual torque.

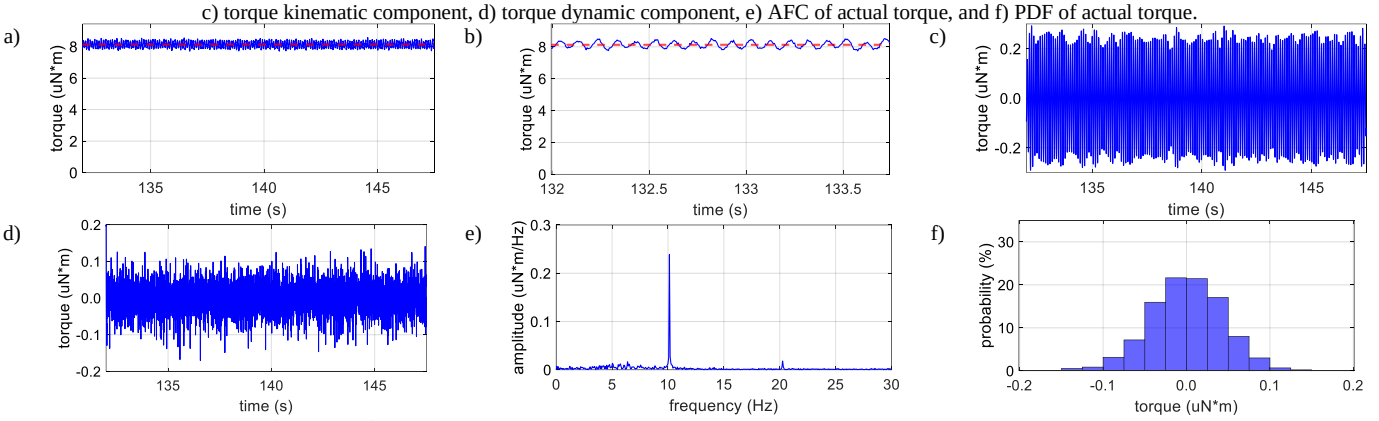

Figure 6. Functional performance of the drum with 45 µm riblets at 63.7 rad/s angular speed: a) actual torque, b) detailed view actual torque variation, c) torque kinematic component, d) torque dynamic component, e) AFC of actual torque, and f) PDF of actual torque.

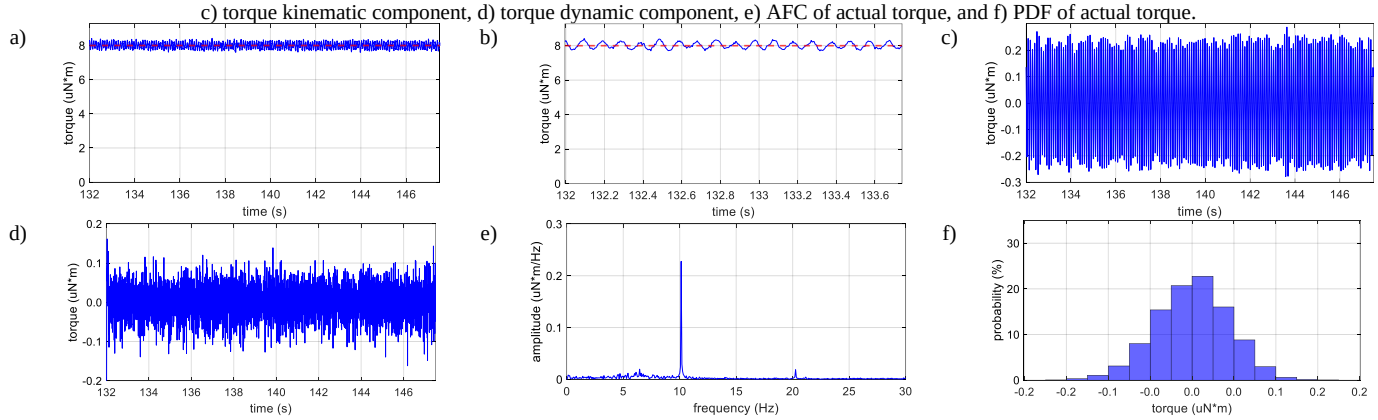

Figure 7. Functional performance of the drum with 65 µm riblets at 63.7 rad/s angular speed: a) actual torque, b) detailed view of the actual torque variation, c) torque kinematic component, d) torque dynamic component, e) AFC of actual torque, and f) PDF of actual torque.